



Swansea University
Prifysgol Abertawe



Cronfa - Swansea University Open Access Repository

This is an author produced version of a paper published in:

Journal of Biomechanics

Cronfa URL for this paper:

<http://cronfa.swan.ac.uk/Record/cronfa35694>

Paper:

van Loon, R. Integrated Geometric and Mechanical Analysis of an Image-Based Lymphatic Valve. *Journal of Biomechanics*

<http://dx.doi.org/10.1016/j.jbiomech.2017.09.040>

This item is brought to you by Swansea University. Any person downloading material is agreeing to abide by the terms of the repository licence. Copies of full text items may be used or reproduced in any format or medium, without prior permission for personal research or study, educational or non-commercial purposes only. The copyright for any work remains with the original author unless otherwise specified. The full-text must not be sold in any format or medium without the formal permission of the copyright holder.

Permission for multiple reproductions should be obtained from the original author.

Authors are personally responsible for adhering to copyright and publisher restrictions when uploading content to the repository.

<http://www.swansea.ac.uk/library/researchsupport/ris-support/>

Accepted Manuscript

Integrated Geometric and Mechanical Analysis of an Image-Based Lymphatic Valve. (Second Revision)

Daniel J. Watson, Igor Sazonov, David C. Zawieja, James E. Moore Jr., Raoul Loon van

PII: S0021-9290(17)30513-4

DOI: <https://doi.org/10.1016/j.jbiomech.2017.09.040>

Reference: BM 8399

To appear in: *Journal of Biomechanics*

Received Date: 12 January 2017

Accepted Date: 25 September 2017

Please cite this article as: D.J. Watson, I. Sazonov, D.C. Zawieja, J.E. Moore Jr., R. Loon van, Integrated Geometric and Mechanical Analysis of an Image-Based Lymphatic Valve. (Second Revision), *Journal of Biomechanics* (2017), doi: <https://doi.org/10.1016/j.jbiomech.2017.09.040>

This is a PDF file of an unedited manuscript that has been accepted for publication. As a service to our customers we are providing this early version of the manuscript. The manuscript will undergo copyediting, typesetting, and review of the resulting proof before it is published in its final form. Please note that during the production process errors may be discovered which could affect the content, and all legal disclaimers that apply to the journal pertain.



Integrated Geometric and Mechanical Analysis of an Image-Based Lymphatic Valve. (Second Revision)

Daniel J. Watson^a, Igor Sazonov^a, David C. Zawieja^b, James E. Moore Jr.^c,
Raoul van Loon^{a,*}

^aZCCE, College of Engineering, Swansea University

^bCollege of Medicine, Texas A&M Health Sciences Center

^cDepartment of Bioengineering, Imperial College London

Abstract

Lymphatic valves facilitate the lymphatic system's role in maintaining fluid homeostasis. Malformed valves are found in several forms of primary lymphoedema, resulting in incurable swelling of the tissues and immune dysfunction. Their experimental study is complicated by their small size and operation in low pressure and low Reynolds number environments. Mathematical models of these structures can give insight and complement experimentation. In this work, we present the first valve geometry reconstructed from confocal imagery and used in the construction of a subject-specific model in a closing mode. A framework is proposed whereby an image is converted into a valve model. An FEA study was performed to identify the significance of the shear modulus, the consequences of smoothing the leaflet surface and the effect of wall motion on valve behaviour. Smoothing is inherent to any analysis from imagery. The nature of the image, segmentation and meshing all cause attenuation of high-frequency features. Smoothing not only causes loss of surface area but also the loss of high-frequency geometric features which may reduce stiffness. This work aimed to consider these effects and inform studies by taking a manual reconstruction and through manifold harmonic analysis, attenuating higher frequency features to replicate lower resolution images or lower degree-of-freedom recon-

*Corresponding author

Email address: R.vanLoon@swansea.ac.uk (Raoul van Loon)

structions. In conclusion, two metrics were considered: trans-valvular pressure required to close the valve, ΔP_c , and the retrograde volume displacement after closure. The higher ΔP_c , the greater the volume of lymph that will pass through the valve during closure. Retrograde volume displacement after closure gives a metric of compliance of the valve and for the quality of the valve seal. In the case of the image-specific reconstructed valve, removing features with a wavelength longer than four μm caused changes in ΔP_c . Varying the shear modulus from 10kPa to 60kPa caused a 3.85 fold increase in the retrograde volume displaced. The inclusion of a non-rigid wall caused ΔP_c to increase from 1.56 to 2.52 cmH_2O

Keywords: lymphatic, valve, harmonic manifold analysis, segmentation, FEA
2010 MSC: 65D18, 65M60

1. Background

The lymphatic system is responsible for maintaining fluid balance within the tissues (Carola et al. (1990)). The collecting lymphatics drain fluid from the interstitial tissues, transport this fluid through valved contractile tubular structures - called lymphangions - before emptying into the venous system (Alitalo
5 (2011)). The valve behaviour is poorly understood and essential for efficient fluid transport against gravity. Insufficient transport can lead to lymphoedema i.e. inflammation and an accumulation of lymph fluid in the tissues. This results in swelling leading to fibrous tissue formation and compromised im-
10 mune function (Penzer (2003); Bellini & Hennekam (2014)). Several authors have commented on the potential benefit of a lumped model of the lymphatic system and attempts to that end have been made (Margaris & Black (2012); Rahbar & Moore Jr. (2011); Macdonald (2008)). Sensitivity analysis of lumped
15 ing function (Jamalian et al. (2013)) as is the trans-valvular pressure required to close the valves (Bertram et al. (2013)).

As far as the authors are aware no numerical analysis greater than 1-D has

been performed to study lymphatic valve closure. A finite volume approach to flow around a 2-D valve has been considered (Macdonald (2008)). Studies
20 have looked at the opening behaviour of three-dimensional parametric valves through mixed finite element and finite volume methods (Wilson et al. (2015)).

However, reconstruction from confocal imagery (Rahbar et al. (2012)) reveals geometric features on the valve that have not been included in previous parametric models (Wilson et al. (2015)). Reconstruction, spectral analysis
25 and finite element analysis of these structures may elucidate their role and allow their inclusion in parametric models. Manifold harmonic analysis of triangulations is analogous to Fourier analysis in signal processing, as it allows a controlled removal of features, that is not possible in other smoothing algorithms.

30 Confocal scans allow for a geometric characterisation of lymphatic valves. This information can be used as a basis for building idealised models, which are well-suited for parametric studies to elucidate a representative valve behaviour with the construction of a lumped model of the lymphatic system as a final goal. This process is intensive, and an idealised representative model would
35 allow large parametric studies to find the relationships necessary to construct a lumped model of the lymphatic system. The presence of wavy features on the surface of the valve poses a problem as they can only be captured with higher order geometric models, which requires more information. Smoothing is inherent to imaging and meshing, but the sensitivity of lymphatic models to
40 surface smoothness has not been established.

This work aimed to provide the first image-specific lymphatic valve geometry and to use a mechanical analysis for studying the closure of these compliant valves. The sensitivity of this model is assessed against smoothing, the shear modulus of the leaflet and the inclusion of a non-rigid wall.

45 2. Methods

2.1. Image Processing and Segmentation

The image set used was produced by confocal imagery of a lymphangion isolated from the mesentery of a rat. A section of lymphatic vessel was extracted and placed in a calcium-free solution to prevent contraction. The vessel
50 was cannulated and loaded intra-luminally with Cell Tracker Green. The lymphangion was pressurised to a trans-mural pressure of 5 cmH₂O and scanned with a Leica AOBs SP2 confocal-multiphoton microscope with an U APO 40.0 x 1.15 W CORR objective. A 100mW 488nm laser was attenuated with an acousto-optical modulator, and acousto-optical beam-splitters were used to
55 select the wavelengths from the emission spectrum between 510-525 μm . A single x - y confocal slice was acquired perpendicular to the axial direction of the vessel, after which the focal plane was advanced along the z -axis before acquiring the next x - y image. The scans represent a pack of 195 2D slices containing 512-by-512 pixels at a resolution of 0.6-by-0.6 μm . The distance
60 between consecutive images was 1 μm . A 307 micron length of wall was segmented from the image set. The valves length was 230 μm from the middle of the bases to the middle of the commissures. The diameter at the commissures was 160 μm , and the diameter at the base was 90 μm . The average thickness of the wall was 14 μm and the average thickness of the leaflet was deemed
65 5 μm by inspection. The valve had a sinus-to-root ratio of 1.78, larger than the mean of 1.65, but still within the observed range of 1.20 to 2.66 (Wilson et al. (2015)).

As can be seen in Figure 1.A, the images were noisy, the objects blurred and the intensity was non-uniform. Intensity decayed exponentially from the
70 surface to the depth of the object due to absorption. These issues complicated the reconstruction of the leaflets, which was ultimately performed manually. The image was then subjected to a median filter. An overview of the lymphatic valve geometry is shown in Figure 2.A and B.

2.1.1. Segmentation of the Wall

75 A custom algorithm for segmenting the wall and reconstructing the leaflets was implemented in MATLAB. The wall was segmented by an automatic active contour method. In order to achieve this, we introduced the Cartesian coordinates; x , representing the horizontal direction in each slice; y , the vertical direction; and z , the depth of a slice. Then wall contours are arranged in every z - y slice, see Figure 1.B. The initial contour in the first z - y slice is an ellipse set manually by four points on the image in the middle of the wall. The contour displaces along its normal, moving up intensity gradients and stopping when it reaches the maximal intensity. In all subsequent slices, the final contour of the previous slice is taken as the initial. Thus the procedure is practically auto-
85 matic except the initialisation of the first four points. As a result, the wall medial surface is recovered and represented as a cloud of points. The local thickness is then determined by examining the decay of the image intensity from the medial surface normal, with the outer and inner surfaces defined as the opposing points of maximal intensity decay. The geometry is then smoothed along the surface to remove noise effects, shown in blue in Figure 1.C. The inner and
90 outer surfaces can be seen in yellow in Figure 1.B-D.

2.1.2. Reconstruction of the leaflets

First, a separation line is drawn between the two leaflets on each slice, see Figure 1.A. This line is then be used to distinguish the leaflets. A z - y and
95 x - y slice with the leaflets coloured red and blue is shown in Figure 1.B and C respectively. The intensity for each coloured leaflet is summed in the z direction creating a 2D image that reveals the outline of the leaflets, shown in Figure 1.D. The trailing edges of the leaflets are traced and used as a guide for manual reconstruction. A vector is constructed such that it is roughly perpendicular to the valve in the z - y plane with the guidelines parallel to this vector as is shown
100 in Figure 1.C. For each slice, the user places a number of vertices resulting in a polygonal chain that describes the shape of the leaflet, see Figure 1.D. These points can then be post-processed and meshed to obtain the final geometry,

see Figure 2.C.

105 2.2. Material Properties

The mechanical response of lymphangions consists of both a passive response, due to the material, and an active response, due to muscular tone and periodic contraction as part of the pumping mechanism. No consideration was given to the contractile nature of lymphangion walls as the imaging was performed in a calcium-free media and complimentary experimental results exist (Davis et al. (2011)). Rahbar et al. (2012) found that the leaflets consist of an elastin network whilst the wall is composed of an collagen-elastin matrix with embedded muscle cells. In the same work, experimentation on rats showed a highly non-linear pressure-diameter relationship for lymphangions given as,

$$P_{mural}(D) = P_{ref} \left(\exp \left[S_p \left(\frac{D}{D_{ref}} - 1 \right) \right] - 0.001 \left(\frac{D}{D_{ref}} \right)^{-3} + 0.05 \right) \quad (1)$$

where P_{mural} represents the transmural pressure in cmH₂O, D represents the vessel diameter in μm , S_p the sharpness of the curve and D_{ref} the normalising diameter measured at $P_{mural} = P_{ref}$. For lymphangion sections taken upstream of valves the mean values for P_{ref} and S_p were 18.0 and 20.4 respectively. It is important to note that the normalising pressure, P_{ref} is the highest pressure observed and thus its associated diameter, D_{ref} , is the largest. Ideally, study toward a constitutive model would take into account fibre orientation, ratio and topology, as has been previously performed for thoracic ducts (Caulk et al. (2015)). However, experimentation is complicated by the small size and the collapse of the wall in a stress-free state. The assumption that the wall is dominant over the leaflets allows a method by which representative wall motion can be achieved. Through an elasto-plastic model where the wall was considered very stiff elastically, and artificial plastic deformation was used to model the non-linear component of the behaviour described in Eq 1. This model reproduces representative wall motion for use in leaflet study only for monotonically increasing pressurisation. Firstly the wall is considered to be a homogenous thin walled cylinder described in $\{\Theta, R\}$ with $0 < \Theta \leq 2\pi$,

$R = r(P_{mural})$ with associated thickness, $t(P_{mural})$; where $r(P_{mural})$ is the radius of the wall at pressure P_{mural} . The assumption of symmetry allows only displacement u in R . The assumption of incompressibility suggests that cross-sectional area is conserved which allows the calculation of $t(P_{mural})$. The principle strains can be written as:

$$\epsilon_{\Theta} = \frac{u}{r(P_{mural})}, \epsilon_R = \frac{t(P_1) - t(P_{mural})}{t(P_{mural})} \quad (2)$$

The principle stresses can be written as:

$$\sigma_{\Theta} = \frac{r(P_{mural})P_{mural}}{t(P_{mural})}, \sigma_R = \frac{-P_{mural}}{2} \quad (3)$$

P_1 represents the transmural pressure at imaging. This allows the creation of a von-Mises equivalent stress-strain relationship. The pre-stress of the cylinder was modelled by the addition of the existing stress with the von-Mises stress, σ_{vM} .

$$\sigma_{vM}(P_{mural}) = \sigma_{vM}(P_1) + \sigma_{vM}(P_{mural} - P_1) \quad (4)$$

This relationship was decomposed into a linear-elastic component with elastic component representing the gradient at $P_{mural} = P_0$, in this case, a modulus of 413 kPa. The remaining strain is modelled through artificial plastic deformation. This model was implemented in *ANSYS Workbench*, and the wall was
 110 pressurised to 18 cmH₂O. Shown below in Figure 3 is the fit described in Eq 1 compared to the mean D/D_{ref} for 10 equally sized bands taken along the z -axis, shown as the coloured wall in Figure 3. As can be seen, the reconstructed wall is slightly more compliant than the fit.

As the leaflets surface does not contain collagen, an incompressible neo-
 115 Hookean model was used for the leaflets with a shear modulus of 45kPa for the smoothing study, see section 2.4. This value has been used in other studies of lymphangions but is based on experimental data from arterial elastin (Wilson et al. (2015)). The sensitivity of this value was assessed in the material properties study.

120 2.3. FEA model set-up

ANSYS Workbench was used to solve the FEA problems. Meshes of varying densities were originally created for the reconstructed geometry. For the smoothing study, these meshes were then converged to a mean 1 percent relative error of displacement for coincident nodes, at a meshing density of 1 node per $3 \mu\text{m}^2$. The results of the manifold harmonic analysis were re-meshed, to preserve mesh quality, at a finer level of 1 node per μm^2 . See Appendix A.1 for more re-meshing details. For the flexible wall studies an initial mesh of 1 node per $5 \mu\text{m}^2$ was refined until the pressure required to close the valve, ΔP_c , and the retrograde displacement of volume both had a relative error of less than one percent. For every mechanical model, the leaflet was represented as a series of linear quadrilateral and triangular shells each with an associated thickness of $5 \mu\text{m}$. Contact between the leaflets was modelled by an augmented Lagrange algorithm; the normal stiffness was relaxed to 0.5 of the default setting to allow convergence and a contact stabilisation damping factor of 0.5 was used. The leaflets were considered rough, and slipping was discouraged through a penalty scheme. A static analysis was performed where a maximum trans-valvular pressure difference of $5 \text{ cmH}_2\text{O}$ was incrementally imposed over 50 steps resulting in valve closure. For the smoothing study, the annulus was fixed in space. For the flexible wall studies the afferent and efferent ends of the wall were held in-plane, and one node on the afferent end of the wall was fixed in space. The leaflets were bound to the wall by coupling displacements to the nearest nodes on the wall. Rotations were also coupled in order to represent collagen buttressing of the leaflet (Rahbar et al. (2012)). After calculation, two metrics were considered, i.e. the trans-valvular pressure required to close the valve and the retrograde volume displacement after closure. Closure was defined as the minimum orifice area calculated by projecting the trailing edge onto an axial plane. The retrograde volume displaced after closure was estimated by comparing integrations between the two leaflets in the imaged state and then after the application of a $5 \text{ cmH}_2\text{O}$ trans-valvular pressure difference in a closing manner. As can be expected, the retrograde volume displaced is a

function ΔP_c , but is also influenced by the compliance of the geometry.

2.4. Smoothing Method

The wall was considered rigid, as only the behaviour of the leaflets due to smoothing was considered. The objective of the manifold harmonic analysis was to perform a low-pass filtering. To remove higher frequency features associated with a subject-specific geometry in a quantifiable manner. This allowed a discussion of geometric valve features and their influence on mechanical valve behaviour. For detail on manifold harmonic transforms see Appendix B. Filters can be applied to the transformed geometry, much like any Fourier transform of an image. By simply truncating the transform, prior to taking the inverse transform, we achieve a low-pass filter (Vallet & Lévy (2008)). By removing high-frequency features from the valve surface, it allows us to differentiate features that affect valve behaviour. To reduce filtering artefacts, a high roll-off low-pass Gaussian filter was used with a defined cut-off frequency, ω_{cut} . From the eigenvalue matrix, we can define a frequency vector, ω . A filter kernel $f(\omega)$ can now be constructed as,

$$f(\omega_i) = \begin{cases} 1 & \text{for } \omega_i < \omega_{cut} \\ e^{-r(\omega_i - \omega_{cut})^2} & \text{for } \omega_i \geq \omega_{cut} \end{cases} \quad (5)$$

where r is a constant related to the roll-off (in this case $r = 10^5$ was used) and $\omega_i = \sqrt{\Omega_{ii}}$ with frequency eigenvalue matrix Ω .

155 3. Results

Using harmonic analysis, the transform of the reconstructed geometry was found and eight filters placed exponentially through the frequency space. For each filter, the transform was inverted, creating a smoothed geometry with high frequency features removed. As shown in Figure 4 the filter points are super-
160 imposed on a magnitude-frequency spectrum of both leaflets. The solid lines represent the apex of the Gaussian filter, and the dashed lines represent the

half-power points. The full cases can be seen in Figure A.2. Two phases of displacement can be identified during the application of an increasing trans-valvular pressure gradient. In Figure 5, the mean of the peak axial displacement of the trailing edge for both leaflets with a flexible wall is shown with two specific regions highlighted. Firstly, the unimpeded motion of the trailing edges toward each other and subsequently a transition where the trailing edges start to coapt together. This leads to the second phase, where the leaflets coapt and the valve seal develops. These regions can be delineated by the first trans-valvular pressure at which contact between the two leaflets occurs, Figure 5.A. Also shown are the pressure of closure as previously defined and the final load-step Figures 5.B,C.

3.1. Leaflet Material Sensitivity Study

A study was performed to assess the sensitivity of the model to changes in leaflet shear modulus. The wall was included in this study to capture a representative wall motion. The shear modulus of the leaflets was varied from 10kPa to 60kPa. A trans-valvular pressure of 5 cmH₂O was applied to close the valve. Shown in Figure 6 are the effects of leaflet shear modulus on the trans-valvular closing pressure of the leaflet, ΔP_c . There is a clear relationship between decreasing stiffness and a reduced ΔP_c . Comparison with experimental data for a comparable valve suggests that the valve shear modulus lies in the range 10-20 kPa (Davis et al. (2011)). After closure of the valve, the leaflets continue to deform axially under the applied trans-valvular pressure, which results in retrograde displacement of the fluid within the lymphangion. The change in retrograde volume displaced at 5 cmH₂O is shown in Figure 8. This metric can be considered a measure of valve compliance as the deformations will be larger for smaller shear moduli resulting in a larger volume displaced.

3.2. Leaflet Smoothing Sensitivity Study

The upper graph of Figure 7 shows the development of the orifice area for an increasing trans-valvular pressure. Due to bending instabilities, many

kinks can be observed in the curve for the original geometry. Less kinks are present in the curves for the smoother valves as the features responsible for these instabilities are removed. The bottom plot of Figure 7 shows the values of ΔP_c at various cut-off frequencies. Whilst ΔP_c generally increases with the removal of features, this relationship is not monotonic. It is clear that a non-trivial relationship exists between the frequency of a feature its effect on valve closure.

4. Discussion

This work demonstrates that it is feasible to reconstruct a lymphatic valve from confocal images. Smoothing the original reconstruction shows that the absolute relative error between the seventh filter and the original geometry is within four percent, see Figure 7. This suggests critical features are those not attenuated by the 8th filter, i.e. those with a wavelength of less than $4.094 \mu\text{m}$. These features could still be discerned at a resolution as low as the Nyquist interval for that filter of approximately $2 \mu\text{m}$ per pixel, which is half of the z resolution of the images used in this study and three-tenths of the resolution in the other directions. Lowering the resolution may be beneficial to the study of real geometries if a coarser image had a higher signal-to-noise ratio. There is a large difference in pressure required to close the valve, ΔP_c , between the second and third smoothest filters, see Figure 7. Whilst it could be argued that this is due to the loss of surface area, the difference in area is 8% between the second and third filter. However, the difference in ΔP_c is smaller between the first and second smoothest filters, whose difference in area is 14%. This suggests there is a geometric feature or features whose wavelength lies between 33.8 and $51.5 \mu\text{m}$, which has a contribution to the behaviour of the valve disproportionate to the surface area it adds.

Comparing the 45 kPa shear modulus case from the material study and the original geometry from the smoothing study, shows the consequences of a non-rigid wall. The change in ΔP_c increases from 1.56 to 2.52 when repre-

220 sentative wall motion is allowed. Given the experimental fit used to generate the wall model, see Eq. 1, predicts a 3.55% increase in diameter for a change in transmural pressure from 5 to 10 cmH₂O it would appear the wall has a significant effect on ΔP_c .

Intuitively, the shear modulus also affects ΔP_c causing a 3.85 fold increase
225 as the leaflet stiffness increases from 10 to 60 kPa. Given previous experimental results it would appear that for ΔP_c to lie within a physiological range of 1.1 to 1.2 cmH₂O (Davis et al. (2011)), then the shear modulus of the leaflet would have to be reduced by more than half.

There are several limitations to this study. The wall model in this study was
230 designed to produce representative motion. The implementation of an experimentally validated constitutive model for the wall would allow for a greater consideration of its behaviour. The contractile nature of the lymphangion wall was not considered and would offer greater insight in lymphatic insufficiency. The estimated shear modulus for the leaflet of 45kPa, based on arterial studies of
235 elastin and similar to previously used values, appears to be an over-estimation (Wilson et al. (2015)). The properties describing the elastin network in lymphatic leaflets are still unknown and will affect valve behaviour. Experimental determination of these properties is very challenging given the small size of the leaflets. Hence, future work could address these limitations by performing
240 a material characterisation of the valves imaged at two distinct pressure states and through a fully coupled two-way fluid-structure interaction study. While a case has been made for the consequences of wavy features on valve behaviour, there is no evidence for their existence in-vivo. They could be an artefact of imaging or be exaggerated by the imaging procedure. The contractile
245 nature of the wall will mean that the wavy features present during contraction differ from those imaged. Muscle cells are absent within the leaflet therefore as the contractions would reduce vessel diameter the leaflets to become compressed and the wavy features to be exaggerated. The consequences of geometry smoothing have been revealed to be non-trivial, and further work should
250 seek to address questions of the existence of such features and methods of

incorporating them into idealised models.

In conclusion, we have reconstructed a lymphatic valve from confocal images and performed a mechanical analysis to elucidate the characteristics during closing. This analysis indicated the three stages of valve closure and demonstrated the influence of wall motion on ΔP_c . A material sensitivity analysis of the wall suggested that the shear modulus of a lymphatic valve is more likely in the range of 10-20kPa in contrast to arterial elastin networks that have been found around 45kPa.

All these findings will provide a better understanding of the lymphatic draining mechanisms and aid the development of lumped models to study larger networks.

Acknowledgements

Part of this work was sponsored by NIH grant U01 HL123420

Author Contributions

DW and RvL performed the finite element analysis and manifold harmonic analysis. IS developed and performed the image processing, segmentation and meshing. DZ provided the image set and guidance on its interpretation. JM, DZ and RvL designed the study. All authors read and approved the final manuscript.

Conflict of Interest

The authors report no conflicts of interest.

Appendix A. Meshing

The polygonal chains describing the centre of the leaflets were processed to form a triangulated mesh for use in finite element analysis. First, the edge wall nodes are moved to the lumen wall surface by the shortest path, or an additional point is inserted on the wall surface. If the closest leaflet point is located at a large distance from the wall; then the angular positions of the wall edge points, relative to the vessel centreline, are smoothed along the vessel axis. The free edge line is smoothed by a method previously described (Sazonov et al. (2011)).

After that, the leaflet lines in every z - y slice are smoothed by the same method with the weighting coefficients proportional to the length of each segment. This modification is necessary to reduce variations in segment length. The new points are then uniformly distributed along every line and approximated by a cubic spline.

Note that point positions have essential variation from slice to slice, i.e. along the vessel axis, see Figure A1.A. A mesh has to be built before the application of the smoothing technique. As the points are organised along lines, the part of the surface between two subsequent lines, i.e. a strip, can be easily triangulated to form a Delaunay triangulation for each strip. Thus the total mesh is not necessarily Delaunay compliant. The boundary nodes, i.e. nodes along the free edge and the wall edge of the leaflet, are located non-uniformly in some places. They are substituted by uniformly distributed points, and the mesh is re-triangulated locally. The mesh needs anisotropic smoothing to preserve the reconstruction in the y and x -axis, whilst sufficiently attenuating variation from slice to slice in the z -axis. Therefore a modification of the Laplace smoothing method is proposed, in which contiguous nodes placed in the same line, are disregarded. The result of such a method is presented in Figure A.1

300 *Appendix A.1. Re-Meshing*

The initial leaflet mesh is too fine, each element spans a single voxel and the total geometry contains 35000 nodes and 64000 elements. The initial mesh is used as a benchmark and for fast re-gridding of the mesh to obtain a range of element sizes necessary to assess convergence of the finite element scheme.

305 To aid this process, every node of the coarser meshes exactly coincides with one of the nodes in the initial fine mesh. In the re-gridding procedure, the fact that mesh nodes are arranged along lines, is actively used.

Appendix B. Smoothing Algorithm

Taubin (2000) first constructed analogues of common image processing functions by analysing the discrete Laplacian of graphs. Lévy (2006) then used the eigenvectors of the Laplace-Beltrami operator as bases for spectral filtering of triangulations. Consider any triangulation with n_v vertices \mathbf{V} and an associated edge list \mathbf{E} . Now a geometric weight matrix \mathbf{W} of size n_v can be defined as,

$$W_{ij} = \begin{cases} \frac{-\cot(\beta(i,j)) + \cot(\hat{\beta}(i,j))}{2} & \text{for } (i,j) \in \mathbf{E} \\ 0 & \text{else} \end{cases} \quad (\text{B.1})$$

$$W_{ii} = -\sum_{j \neq i} (W_{ij}) \quad (\text{B.2})$$

where $\beta(i,j)$ and $\hat{\beta}(i,j)$ are the measures of the angles opposing the edge (i,j) . A diagonal matrix, \mathbf{D} , can be defined where \mathbf{D}_{ii} equals the finite Voronoi area of the i^{th} member of \mathbf{V} , calculated using the method described by Meyer et al. (2003). The Laplace-Beltrami operator can now be defined as $\mathbf{\Delta} = \mathbf{D}^{-1}\mathbf{W}$. However, it may not be symmetric thus the following symmetric generalised eigenvector problem is solved $\mathbf{W}\mathbf{\Phi} = \mathbf{\Omega}\mathbf{\Phi}\mathbf{D}$ (Reuter et al. (2009)). Which yields a n_v -by- n_v matrix of eigenvectors $\mathbf{\Phi}$, and the eigenvalue matrix, $\mathbf{\Omega}$, whose diagonal, $\mathbf{\Omega}_{ii}$, corresponds to the square of the fundamental frequencies those bases represent. We can thereby transform \mathbf{V} to give $\hat{\mathbf{V}} = \langle \mathbf{V}, \mathbf{\Phi} \rangle_{\mathbf{D}}$

with $\hat{\mathbf{V}}$ the spectral representation and with $\langle \mathbf{A}, \mathbf{B} \rangle_D$ as the D normalised inner product of \mathbf{A} and \mathbf{B} , i.e. $\mathbf{A}^T \mathbf{D} \mathbf{B}$.

The new set of vertices, \mathbf{Y} , can now be found as below.

$$\mathbf{Y} = (f(\boldsymbol{\omega}) \otimes \Phi)^T \langle \mathbf{V}, \Phi \rangle_D \quad (\text{B.3})$$

Upon the boundaries, only one angle opposing the edge is found. Hence, $\cot(\hat{\beta}(i, j))$ does not exist, and only the finite Voronoi region is considered thus creating a Neumann boundary condition (Lévy (2006)). The use of a Dirichlet boundary condition was considered, but as the wavy features are also present on the boundary, the smoothing of the domain would create transitional features between the wavy boundary and the smoothed domain. This was considered unrepresentative of the problem. However, the use of Neumann boundary conditions makes the issue of area loss more acute.

References**References**

- Alitalo, K. (2011). The lymphatic vasculature in disease. *Nature Medicine*, 17, 1371–1380. doi:10.1038/nm.2545.
- Bellini, C., & Hennekam, R. C. (2014). Clinical disorders of primary malfunctioning of the lymphatic system. In F. Kiefer, & S. Schulte-Merker (Eds.), *Developmental Aspects of the Lymphatic Vascular System* (pp. 187–204). Vienna: Springer Vienna. doi:10.1007/978-3-7091-1646-3_14.
- Bertram, C. D., Macaskill, C., Davis, M. J., & Moore Jr., J. E. (2013). Development of a model of a multi-lymphangion lymphatic vessel incorporating realistic and measured parameter values. *Biomechanics and Modeling in Mechanobiology*, 13, 401–416. doi:10.1007/s10237-013-0505-0.
- Carola, R., Noback, C. P., & Hartley, J. P. (1990). *Human Anatomy and Physiology*. (International ed.). New York: McGraw-Hill.
- Caulk, A. W., Nepiyushchikh, Z. V. Shaw, R., Dixon, J. B. & Gleason, R. L. (2015) Quantification of the passive and active biaxial mechanical behaviour and microstructural organization of rat thoracic ducts. *Journal of the Royal Society Interface*, 12(108), doi:10.1098/rsif.2015.0280.
- Davis, M. J., Rahbar, E., Gashev, A. A., Zawieja, D. C., & Moore Jr., J. E. (2011). Determinants of valve gating in collecting lymphatic vessels from rat mesentery. *American Journal of Physiology - Heart and Circulatory Physiology*, 301, 48–60. doi:10.1152/ajpheart.00133.2011.
- Jamalian, S., Bertram, C. D., Richardson, W. J., & Moore Jr, J. E. (2013). Parameter sensitivity analysis of a lumped-parameter model of a chain of lymphangions in series. *American Journal of Physiology - Heart and Circulatory Physiology*, 305, H1709–H1717. doi:10.1152/ajpheart.00403.2013.

- Lévy, B. (2006). Laplace-beltrami eigenfunctions towards an algorithm that understands geometry. In *Shape Modeling and Applications. SMI 2006. IEEE International Conference* (pp. 13–26). doi:10.1109/SMI.2006.21.
- 345
- Macdonald, A. (2008). *The Computational Modelling of Collecting Lymphatic Vessels*. PhD thesis University of Exeter.
- Margaris, K. N., & Black, R. A. (2012). Modelling the lymphatic system: challenges and opportunities. *Journal of The Royal Society Interface*, 9, 601–
- 350 612. doi:10.1098/rsif.2011.0751.
- Masson, I., Boutouyrie, P., Laurent, S., Humphrey, J. D., & Zidi, M. (2008). Characterization of arterial wall mechanical behavior and stresses from human clinical data. *Journal of Biomechanics*, 41, 2618 – 2627. doi:10.1016/j.jbiomech.2008.06.022.
- 355 Meyer, M., Desbrun, M., Schrader, P., & Barr, A. H. (2003). Discrete differential-geometry operators for triangulated 2-manifolds. In H.-C. Hege, & K. Polthier (Eds.), *Visualization and Mathematics III Mathematics and Visualization* (pp. 35–57). Springer Berlin Heidelberg. doi:10.1007/978-3-662-05105-42.
- Penzer, R. (2003). Lymphoedema. *Nursing Standard*, 17, 45–51.
- 360 doi:10.7748/ns2003.05.17.35.45.c3392.
- Rahbar, E., & Moore Jr., J. E (2011). A model of a radially expanding and contracting lymphangion. *Journal of Biomechanics*, 44, 1001 – 1007. doi:10.1016/j.jbiomech.2011.02.018.
- 365 Rahbar, E., Weimer, J., Gibbs, H., Yeh, A. T., Bertram, C. D., Davis, M. J., Hill, M. A., Zawieja, D. C., & Moore Jr., J. E. (2012). Passive pressure diameter relationship and structural composition of rat mesenteric lymphangions. *Lymphatic Research and Biology*, 4, 152–163. doi:10.1089/lrb.2011.0015.
- Reuter, M., Biasotti, S., Giorgi, D., Patané, G., & Spagnuolo, M. (2009). Discrete Laplace-Beltrami operators for shape analysis and segmentation.

- 370 *Computers & Graphics*, 33, 381 – 390. doi:10.1016/j.cag.2009.03.005.
IEEE International Conference on Shape Modelling and Applications 2009.
- Sazonov, I., Yeo, S. Y., Bevan, R. L. T., Xie, X., van Loon, R., & Nithiarasu, P.
(2011). Modelling pipeline for subject-specific arterial blood flow a review.
International Journal for Numerical Methods in Biomedical Engineering, 27,
375 1868–1910. doi:10.1002/cnm.1446.
- Taubin, G. (2000). Geometric signal processing on polygonal meshes. In *Eurographics*.
- Vallet, B., & Lévy, B. (2008). Spectral geometry processing with manifold harmonics. In *Computer Graphics Forum (Proceedings Eurographics)*.
- 380 Wilson, J. T., van Loon, R., Wang, W., Zawieja, D. C., & Moore Jr., J. E.
(2015). Determining the combined effect of the lymphatic valve leaflets and sinus on resistance to forward flow. *Journal of Biomechanics*, 48, 3584 – 3590. doi:10.1016/j.jbiomech.2015.07.045.

Figure 1: A series of z-y slices illustrating a step by step overview of the segmentation process. A) A z-y image slice. B) A segmentation of the wall (yellow). C) The guidelines of leaflet edges used in reconstruction (cyan). D) Manual reconstruction of the leaflet structures (red and blue).

Figure 2: An overview of the lymphatic valve configuration and nomenclature. A) Nomenclature for the valve leaflets. B) The configuration of the leaflets to form the valve. C) Shows the Segmented structures of a subject-specific valve. Leaflets are shown in red and green, and the wall is shown in blue.

Figure 3: A plot of the mean D/D_{ref} for ten equally spaced bands throughout z-axis during pressurisation; also shown is the fit for experimental data found by Rahbar et al.

Figure 4: Magnitude-frequency spectrum with filter cut-off frequencies superimposed solid lines indicate filter apex, dashed lines indicate half power points. Red and blue indicate the two leaflets. The blue dots overlay the red.

Figure 5: A plot of the peak axial displacement of the trailing edge against trans-valvular pressure. Also shown is the original valve at three different trans-valvular pressures with the Euclidean displacement field coloured. A marks the first contact between the leaflets. B marks the point of minimal orifice area and C is the maximum applied trans-valvular pressure.

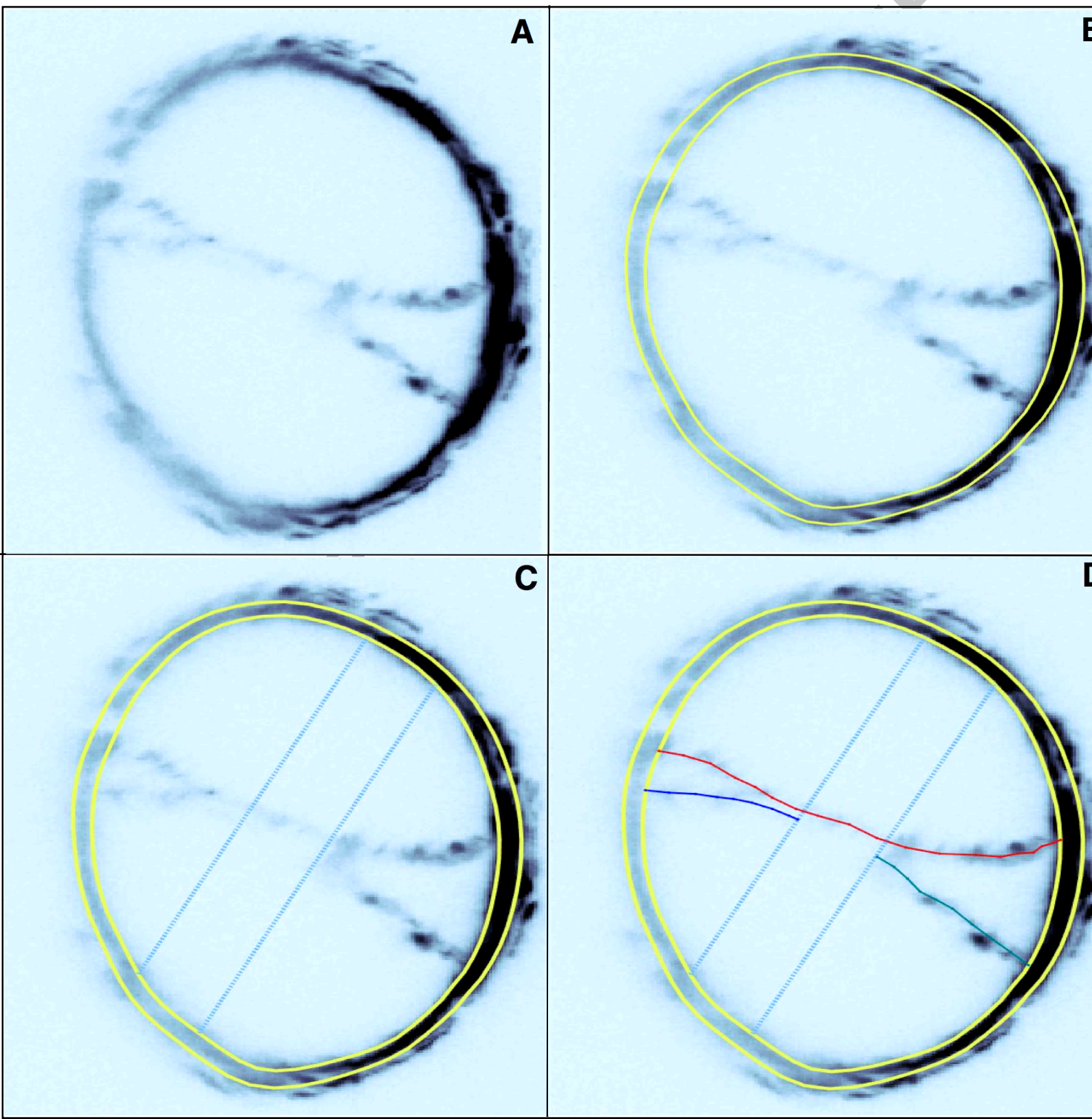
Figure 6: Trans-valvular pressure required to close the valve for differing leaflet shear moduli. The black lines represent the range of trans-valvular closing pressures from experimental data for a lymphatic valve without tone and a trans-mural pressure of 5 cmH₂O

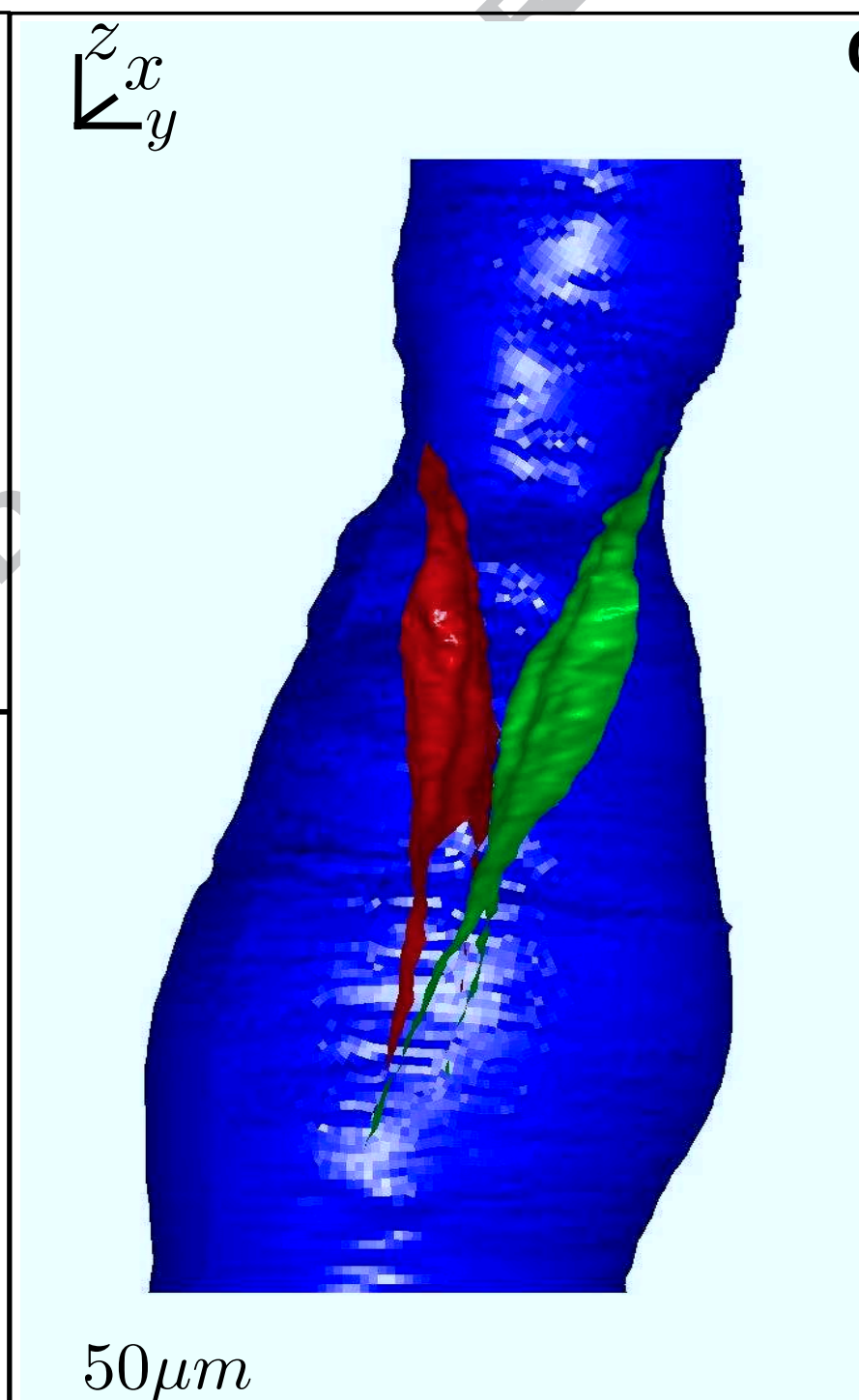
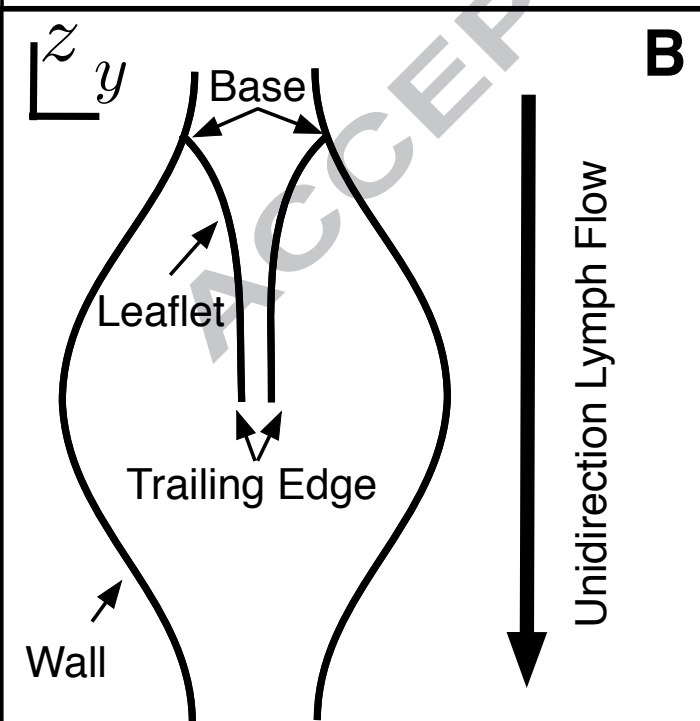
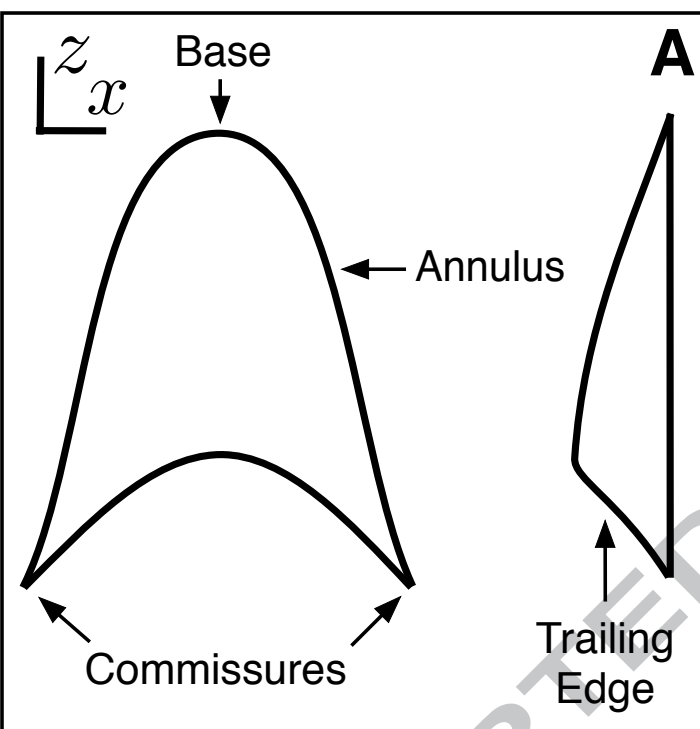
Figure 7: Top: The relative change in the area of the axial projection of the orifice with load. Bottom: The trans-valvular pressure required to close the valve against ω_{cut} the filter cut-off frequency. Note: The top plot is sampled once per 0.1 cmH₂O the kinks are due to bending instabilities

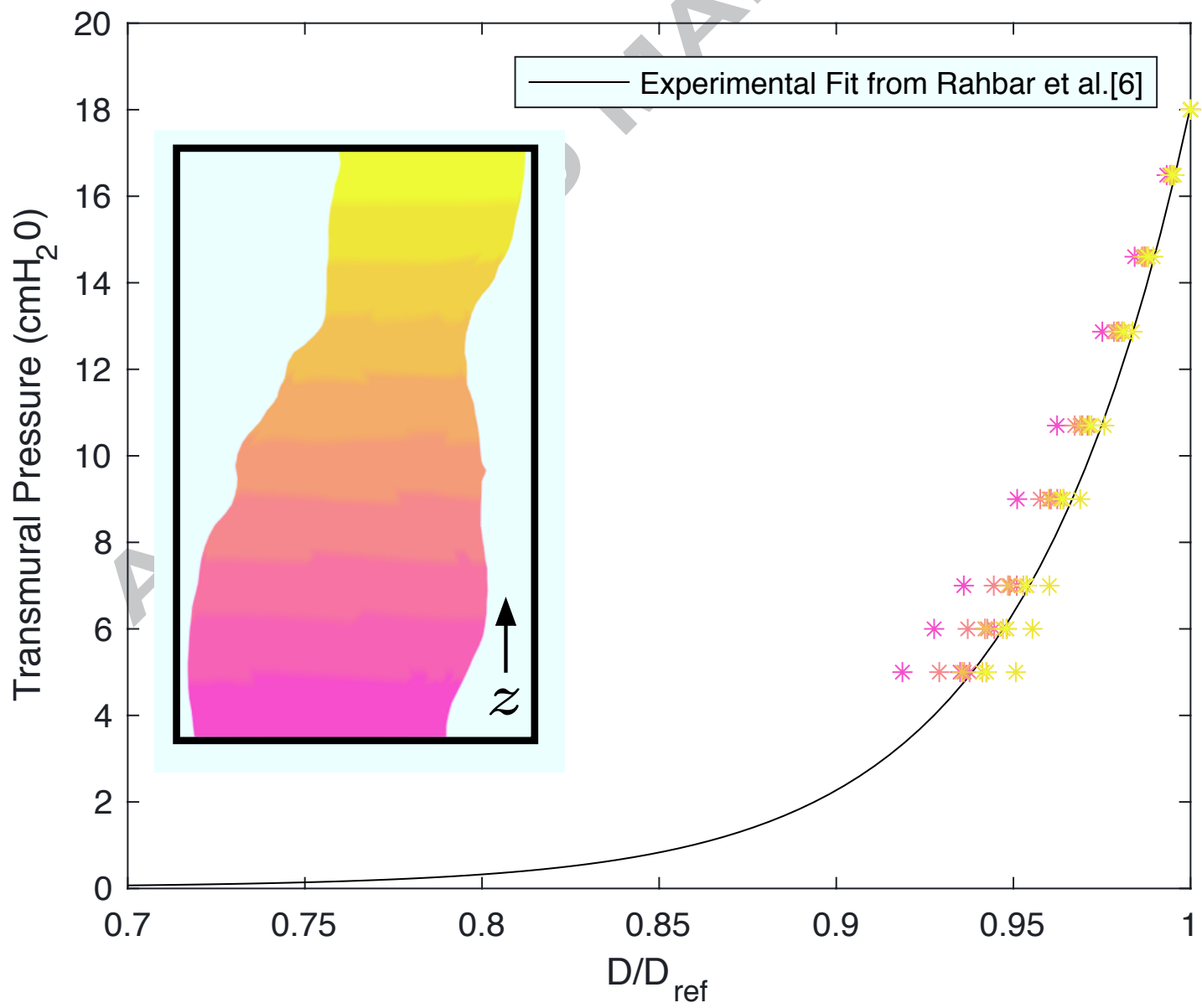
Figure 8: The retrograde volume displaced for differing leaflet shear moduli after the valve has closed. Also shows 2D sketch illustrating the volume in question.

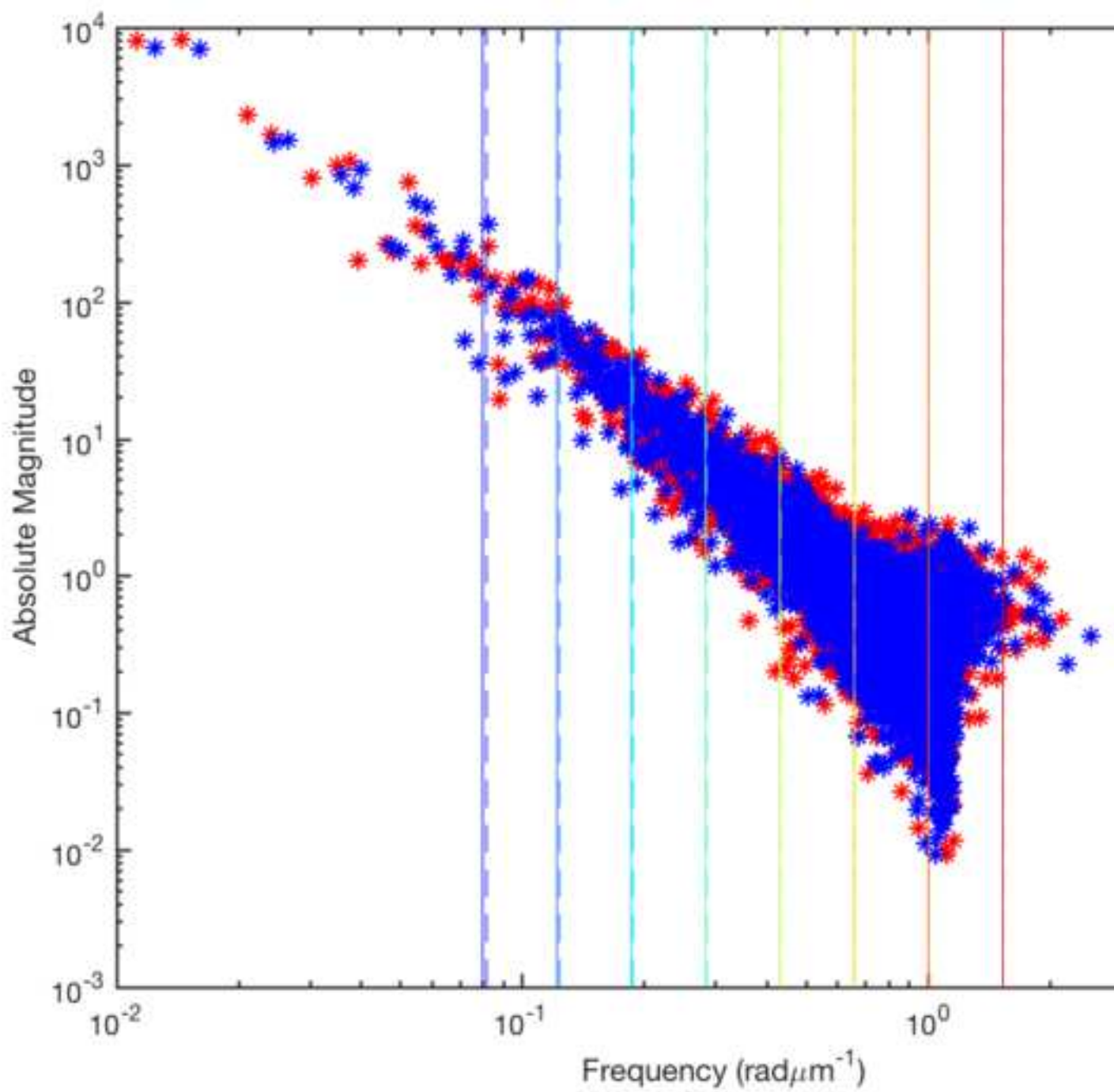
Figure A.1: Smoothing manual reconstruction. Variation in colour represents variation in the surface normal direction. A) The meshed leaflet before smoothing. B) The meshed leaflet after smoothing.

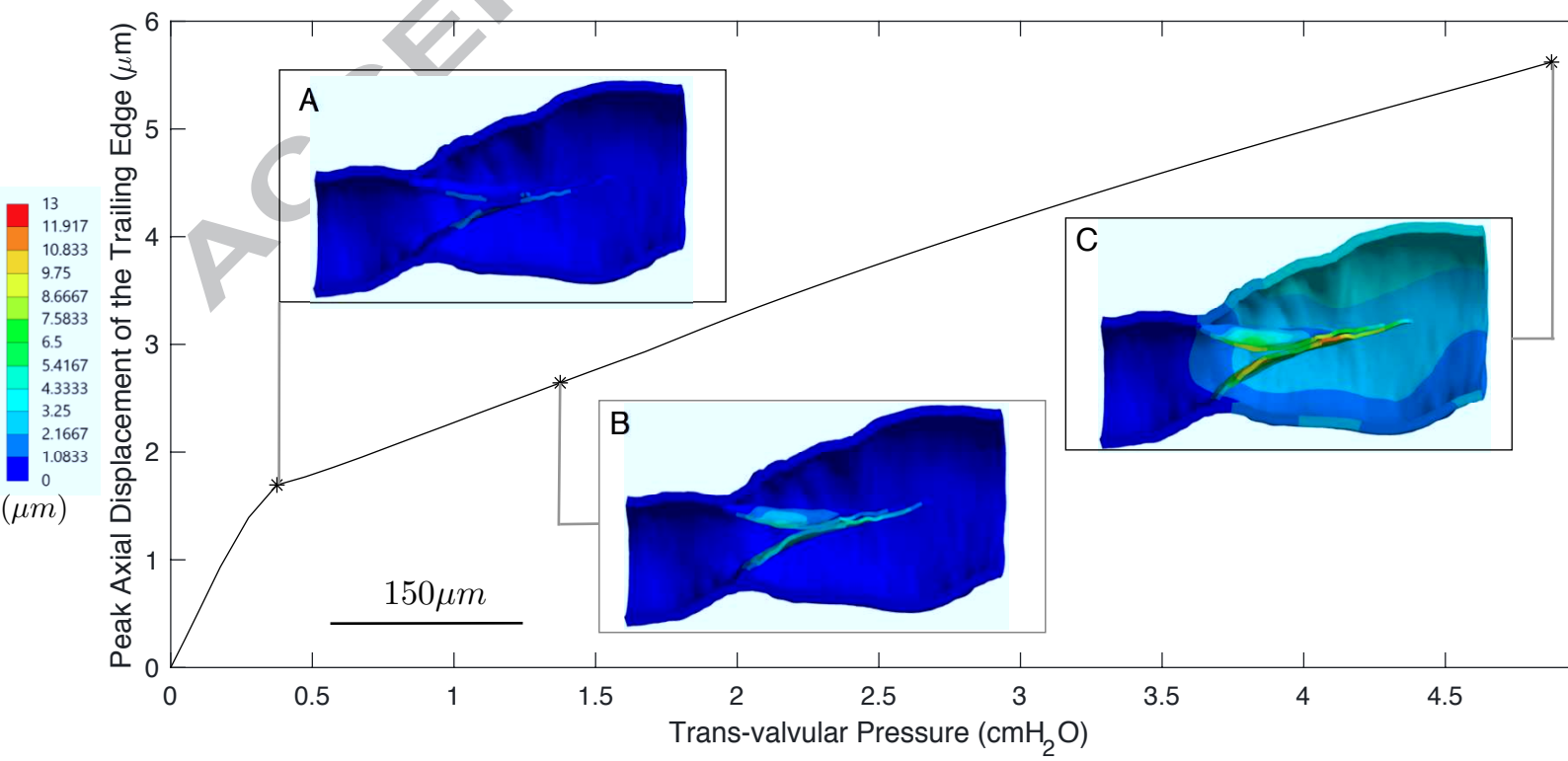
Figure A.2: Geometries produced by filtering the reconstructed leaflets. Top: leaflet 1. Bottom: leaflet 2. Frequencies in $\text{rad } \mu\text{m}^{-1}$











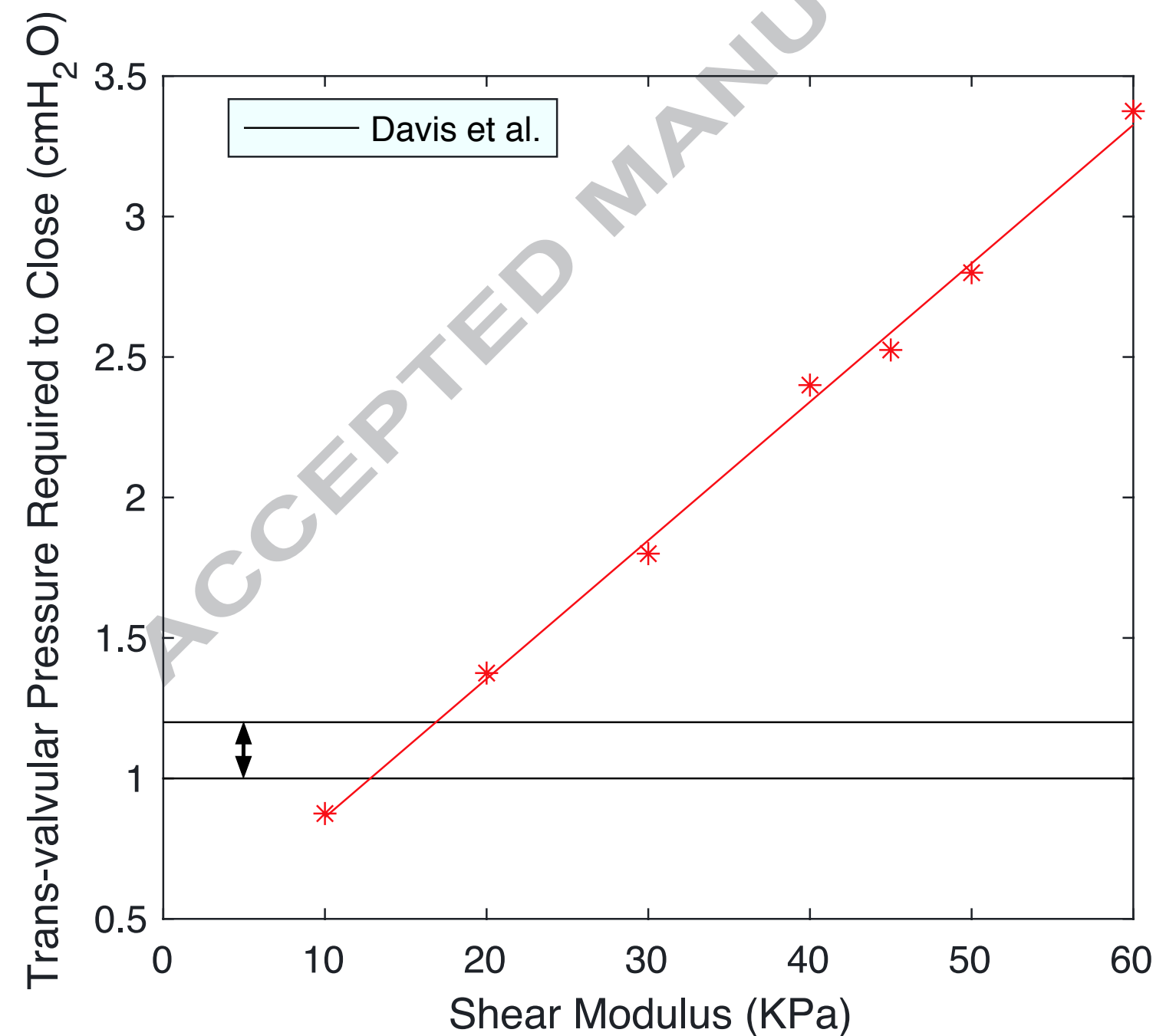
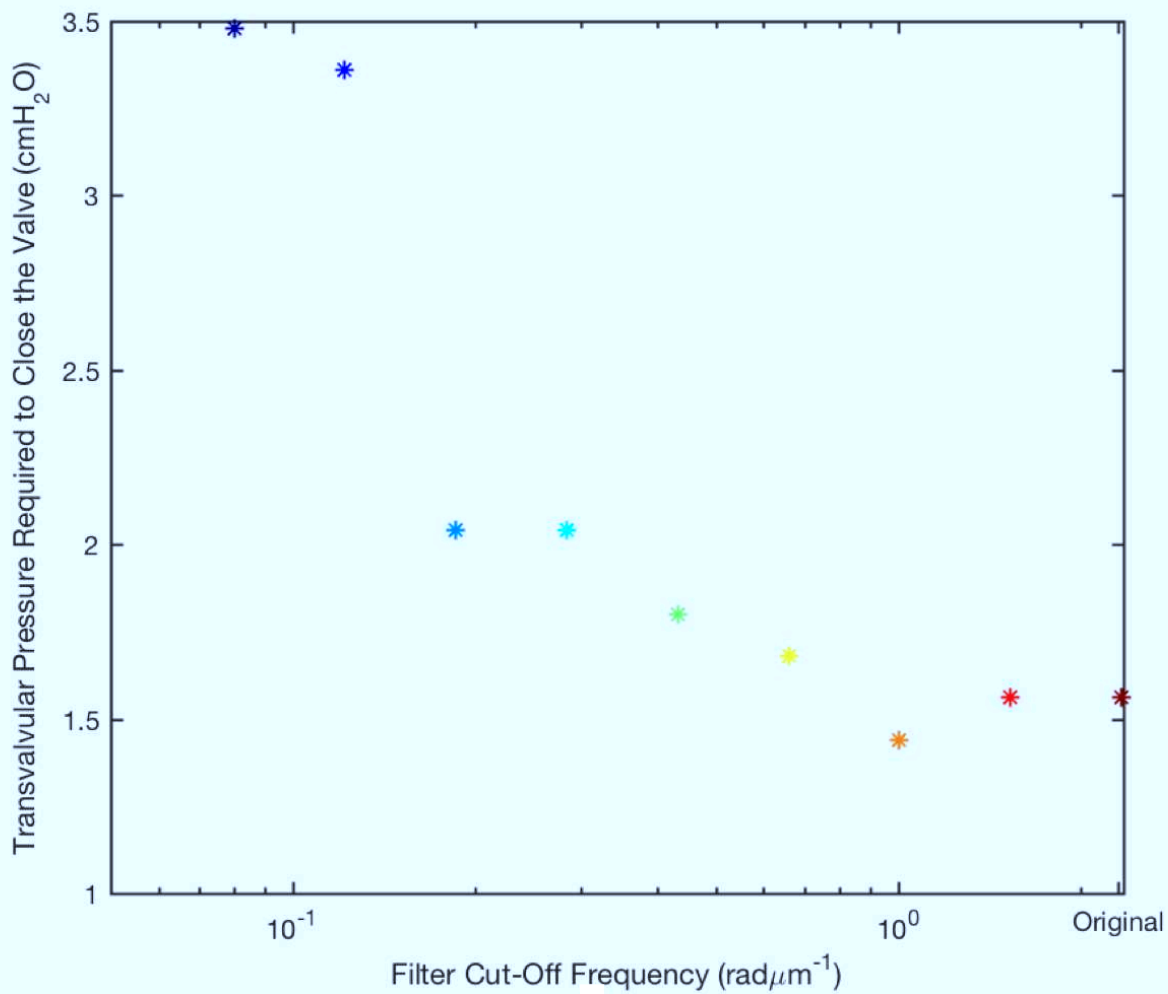
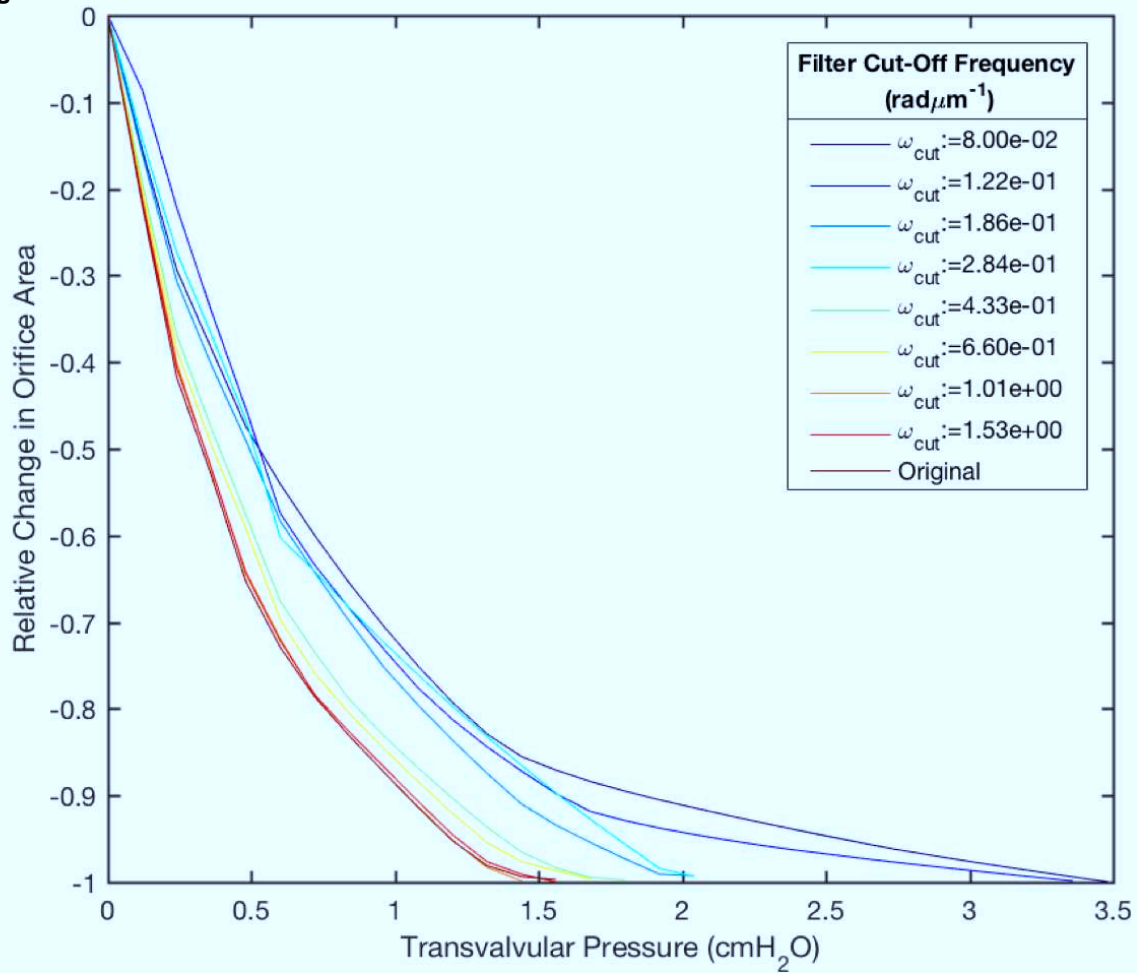
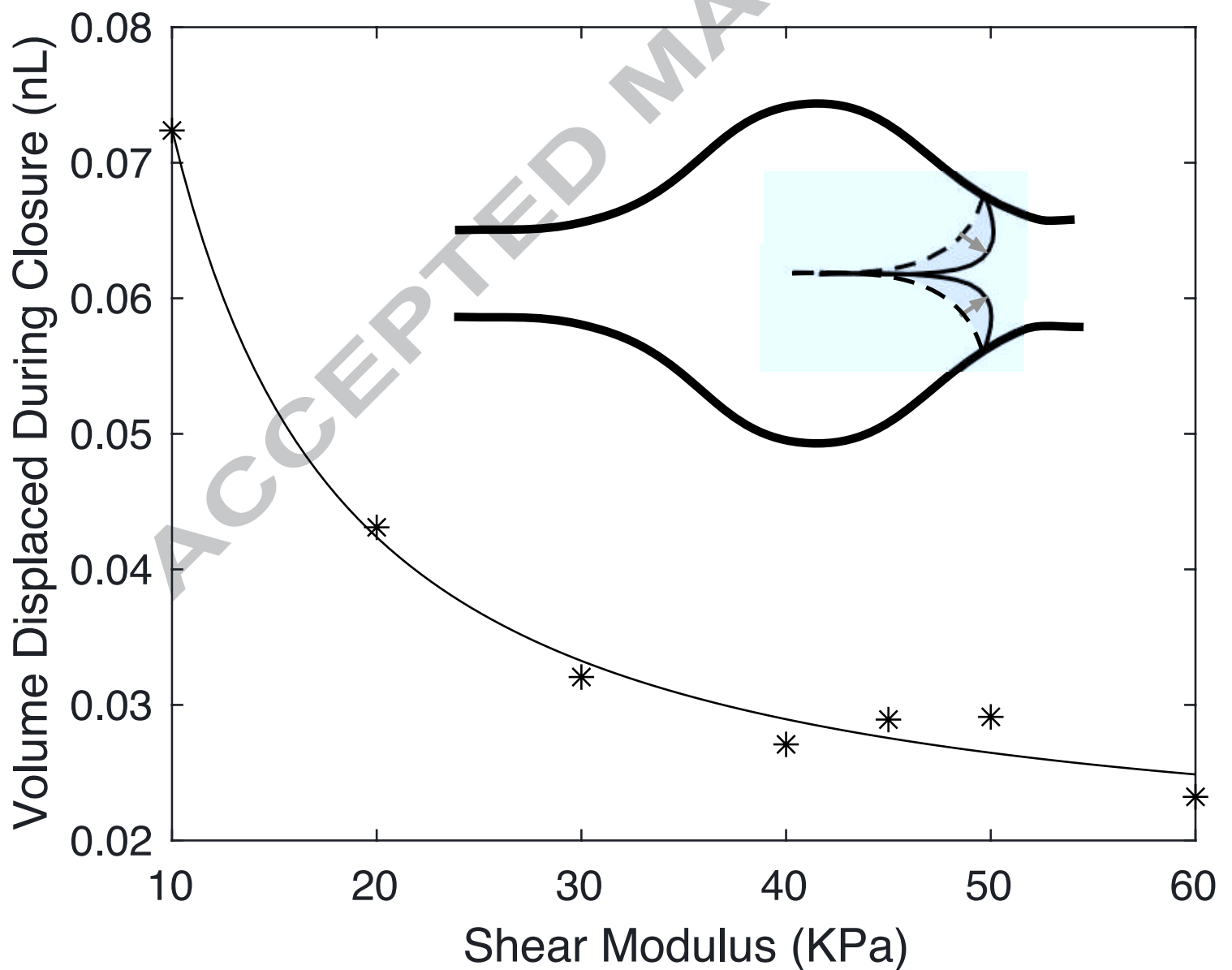


Figure 7



Smooth ←————→ Original

RIPT



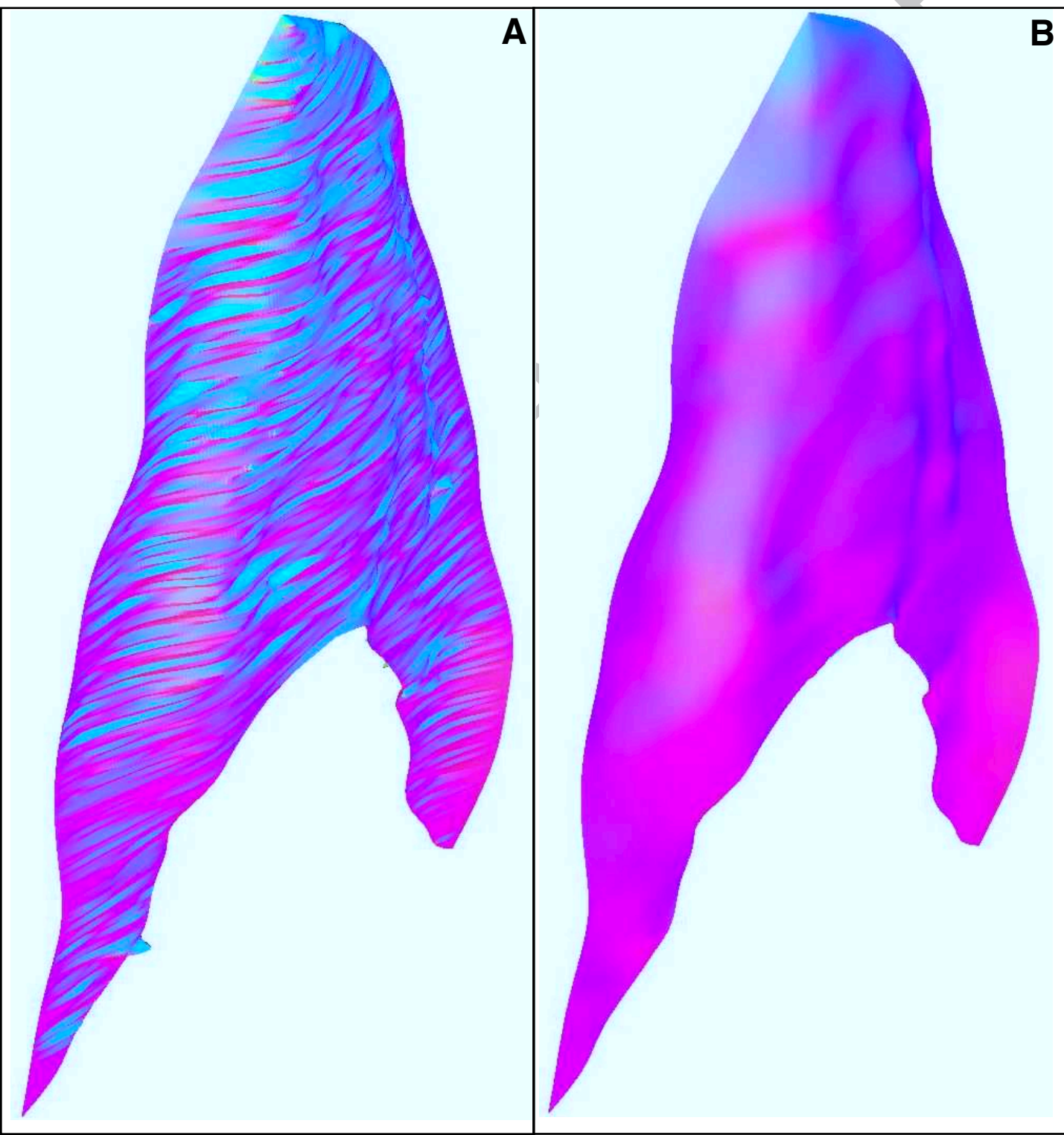


Figure A2

